

Temperature Dependence of Self-diffusion in Cr_2O_3 from First Principles

Bharat Medasani^{b,1}, Maria L. Sushko^b, Kevin M. Rosso^b, Daniel K. Schreiber^c, Stephen M. Bruemmer^c

^aPhysical and Computational Sciences Directorate, Pacific Northwest National Laboratory, Richland, WA 99354, USA

^bDelaware Energy Institute, University of Delaware, Newark, DE 19702, USA

^cEnergy and Environment Directorate, Pacific Northwest National Laboratory, Richland, WA 99354, USA

Abstract

Understanding and predicting the dominant diffusion processes in Cr_2O_3 is essential to its optimization for anti-corrosion coatings, spintronics, and other applications. Despite significant theoretical effort in modeling defect mediated diffusion in Cr_2O_3 the correlation with experimentally measured diffusivities remains poor partly due to the insufficient accuracy of the theoretical approaches. Here an attempt to resolve these discrepancies is made through high accuracy density functional theory simulations coupled with grand canonical formalism of defect thermochemistry. In this approach, point defect formation energies were computed using hybrid exchange correlation functional. This level of theory proved to be essential for achieving the agreement with experimental self-diffusion coefficients. The analysis of the resulting self-diffusion coefficients indicate that chromium has higher mobility at low temperatures and high oxygen partial pressures, in particular at standard temperature and pressure conditions. At high vacuum, high temperature conditions, oxygen diffusion becomes dominant. At $\text{Cr}/\text{Cr}_2\text{O}_3$ interfaces O vacancies were found to be more mobile than Cr vacancies at all temperatures. Cr diffuses preferentially along the c-axis at low temperatures but switches to basal plane at higher temperatures. O diffusion is primarily bound to basal plane at all temperatures.

1. Introduction

Cr_2O_3 finds applications in both functional and structural applications such as catalysis [1, 2], electro-optics[3, 4], magnetoelectronic [5, 6], and corrosion protection[7]. It serves as a protective oxide coating on widely used high-temperature Ni and Fe alloys[8, 9, 10]. Point defects play an important role in the effectiveness of Cr_2O_3 for corrosion protection and other applications and significant experimental effort has been devoted to understanding the nature of point defects and their diffusion mechanisms. However, there is a large spread in the reported self-diffusion coefficients and defect formation energies from various experimental studies [11, 12, 13, 14, 15, 16, 17, 18, 19, 20].

Complementing the experimental investigations, diffusion mediated by both intrinsic and extrinsic point defects in Cr_2O_3 have been extensively studied theoretically by many groups, including ours [21, 22, 23, 24, 25, 26, 27, 28]. Due to the advances in density functional theory (DFT) accuracy in calculating many properties of materials, recent studies employed DFT to evaluate formation energies, migration barriers and charge localization of point defects[22, 23, 24, 28, 27]. The 0K energies obtained from DFT were combined with Einstein-Smoluchowski random walk thermal diffusion formalism[29] to predict the self-diffusion coefficients in Cr_2O_3 . However, the agreement between calculated and experimental self-diffusion coefficients had, so far, been poor, which prompted the use of modified diffusion equations [27, 22]. This leaves the question of the root cause of the discrepancy between theory and experiment unresolved.

A possible source of discrepancy is the insufficient accuracy of the DFT in modeling transition metal oxides, which requires the use of empirical corrections to the exchange-correlation functionals to induce electron localization. For example, to correct for the self-interaction error and induce electron localization in modeling Cr_2O_3 highly correlated Cr-3d (and sometimes O-2p) electrons the Hubbard on-site correction is often employed [30, 31, 32]. However, the resulting defect formation energies vary significantly [22, 23, 24, 25, 20, 33] depending on the choice of Hubbard

*Corresponding author: B. Medasani (mbkumar@udel.edu, mbkumar@gmail.com).

U parameters and the type of the semi-local generalized gradient approximation (GGA) functionals. Adding to the confusion, corrections to minimize the electrostatic errors inherent in the periodic supercell formulation of defects and the errors due to the under-prediction of bandgap by semi-local functionals were either not applied or inconsistently applied in many of these studies.

Rak and Brenner found that the barrier energies for defect migration were not sensitive to the variations in U value. In contrast, they showed that varying U value results in a variation of defect formation energies [27]. The likely reason for such variations is in electronic dissimilarities in the local environments in defected and bulk systems. For example, the electronic density surrounding a point defect such as a vacancy is much lower compared to the electronic density in the corresponding bulk system and the relative effect of U is different.

Selecting the U parameter in the Hubbard correction scheme is neither trivial nor consistent. Often, U selection is based on fitting a bulk property to the experimental value. The chosen optimal U value is highly dependent on the selected bulk property. Another approach which avoids the empirical route in the selection of U is based on the linear response theory (LRT)[34]. LRT based U values often tend to be smaller than the U values obtained from regressing bulk properties. To overcome the uncertainties associated with the empirical U value of Hubbard correction scheme, we employed hybrid functional to accurately evaluate defect electronic levels and defect formation energies.

Here we report self-diffusion coefficients computed using Einstein-Smoluchowski formalism and high accuracy point defect energies. The resulting diffusion coefficients have a reasonable agreement with the experimental data. This work can be considered as the culmination of our previous studies on the atomistic diffusion mechanisms in Cr₂O₃ mediated by vacancies and interstitials [23, 28]. For barrier energies, the transition state and ground defect state exhibit similar local electronic environment, suggesting an insensitivity to the U value used in this prior work. Hence, by utilizing the transition barrier energies obtained in those studies in addition to the revised more accurate defect energies and defect thermodynamics, we evaluated Fermi level variations, stoichiometry deviations and self diffusion coefficients in undoped bulk Cr₂O₃ as a function of temperature and oxygen partial pressure. The computed self diffusion coefficients were analyzed using Brouwer diagrams to reveal the dominant defects responsible for diffusion.

2. Methods

2.1. Density Functional Theory Approach

Density functional theory (DFT) calculations for defect formation energies were performed using the Vienna *ab initio* simulation package (VASP) [35, 36, 37]. We utilized HSE [38] hybrid functional with 25% mixing of Hartree - Fock exchange at short range and 100% PBE correlation. Projector augmented wave (PAW) [39, 40] optimized for PBE [41] functional was used. Wave functions preoptimized from GGA+U calculations with PBEsol [42] functional was used as input to the HSE calculations. The HSE screening parameter of 0.6, which is different from the commonly used values of 0.2 and 0.3 corresponding to HSE06 and HSE03, respectively, was chosen after fitting the computed bandgaps with the experimental bandgap. This point is further discussed in the Results section. The reciprocal space of the primitive cell of Cr₂O₃ ($R\bar{3}c$ space group) with 10 atoms was sampled with 5×5×5 Γ -centered k -point grid. The primitive cell was fully relaxed (both size and shape were relaxed) until the forces converged to 0.01 eV/Å. The atomic positions in the 2×2×1 defect supercells were relaxed at constant volume and fixed cell shape until the individual forces on each atom were minimized to 0.03 eV/Å. For supercell calculations, a cut-off value of 400 eV was used for the plane-wave basis set and 2×2×1 Γ -centered k -point grid was used to sample the reciprocal space. Spin polarization with anti-ferromagnetic (AFM) ordering of Cr spins was used. Gaussian method with a width of 0.01 eV was used for electronic smearing.

2.2. Diffusion Coefficient Calculation

In materials which support charged defects, the diffusion coefficient of an element s can be defined as

$$D_s = \sum_X \sum_q d(X_s^q) \quad (1)$$

where d is the diffusion coefficient pertaining to a defect X_s^q , with X denoting the defect type, and q representing the defect charge. X can be a regular point defect, such as a vacancy or an interstitial, or it can be a complex defect, such

as the Frenkel defect. Based on Einstein's random walk theory, d can be computed as

$$d = \frac{1}{2} c \sum_p m_p l_p^2 \Gamma_p. \quad (2)$$

Here c is the concentration of defect, X_s^q , and p represents one of the migration pathways. m_p , l_p , and Γ_p indicate the multiplicity, length, and jump frequency associated with path p , respectively. The defect concentration, c , is a function of the defect formation energy E_f ,

$$c = c_0 e^{-\beta E_f}, \quad (3)$$

where c_0 is the number of lattice sites per cell volume. According to Vineyard's transition state theory (TST) [43], the jump frequency is defined as a function of the attempt frequency ν_p and the migration barrier energy $E_{m,p}$ as

$$\Gamma_p = \nu_p e^{-\beta E_{m,p}}. \quad (4)$$

The attempt frequency is evaluated under harmonic approximation using the phonon modes of defect ground and transition states as

$$\nu = \frac{\prod_i^{3N-3} \nu_i}{\prod_i^{3N-4} \nu'_j}, \quad (5)$$

where ν_i and ν'_j represent the real phonon frequencies of the ground and transition states of the defect respectively and N is the number of atoms in the bulk supercell.

3. Finite Temperature Defect Concentrations

The effect of pressure and temperature is accounted for in the diffusion coefficients through the chemical potential term in the expression for defect formation energies. Assuming dilute concentrations for defects, we utilized constrained grand canonical formalism to compute the elemental chemical potentials at finite temperatures. This formalism has been successfully applied to predict defect concentrations in ZrO_2 under dilute conditions[44]. In this formalism, bulk Cr_2O_3 is assumed to be in contact with an infinite O_2 reservoir at temperature T and partial pressure p_{O_2} . The oxygen chemical potential then is defined as

$$\mu_{\text{O}}(p_{\text{O}_2}, T) = \mu_{\text{O}}^0 + \Delta\mu_{\text{O}}^0(1\text{atm}, 298\text{K}) + \Delta\mu_{\text{O}}(p_{\text{O}_2}, T). \quad (6)$$

In the above equation, μ_{O}^0 is the 0 K DFT computed O chemical potential, $\Delta\mu_{\text{O}}^0(1\text{atm}, 298\text{K})$ is the correction to obtain the experimental chemical potential of O at standard temperature and pressure (STP: 273 K and 1 atm pressure) conditions, and $\Delta\mu_{\text{O}}(p_{\text{O}_2}, T)$ is given by

$$\Delta\mu_{\text{O}}(p_{\text{O}_2}, T) = kT \ln(p_{\text{O}_2}). \quad (7)$$

The latter two quantities are obtained from NIST-JANAF tables[45]. Cr chemical potential is obtained from μ_{O} as

$$\mu_{\text{Cr}}(p_{\text{O}_2}, T) = \Delta H_{\text{Cr}_2\text{O}_3} - \mu_{\text{O}}(p_{\text{O}_2}, T), \quad (8)$$

where $\Delta H_{\text{Cr}_2\text{O}_3}$ is the formation enthalpy of Cr_2O_3 .

Since the overall system is charge neutral, we impose the charge neutrality condition after accounting for the charged defects and free carriers such as electrons and holes using the expression

$$\sum_{X_s^q} q c^{X_s^q} + p - n = 0, \quad (9)$$

where p and n represent the number densities of holes and electrons, respectively. Given that the formation energy of a charged defect can be calculated as [23, 28]

$$E_f^{X_s^q} = E_{\text{tot}}^{X_s^q} - E_{\text{tot}}^{\text{bulk}} + \sum_{s'} n_{s'}(X_s^q) \mu_{s'} + q E_F + E_{\text{corr}}^{X_s^q}. \quad (10)$$

We can rewrite the concentration of defect X_s^q as

$$c^{X_s^q}(p_{\text{O}_2}, T, E_F) = c_0^{X_s^q} e^{-E_f^{X_s^q}(p_{\text{O}_2}, T, E_F)/kT}. \quad (11)$$

Table 1: Bandgap of Cr₂O₃ obtained with different values of HSE functional screening parameter.

μ	Bandgap (eV)
0.2	4.27
0.3	3.85
0.4	3.64
0.5	3.59
0.6	3.38

Table 2: Bulk properties of Cr₂O₃ obtained with HSE functional.

Property	This Work	Literature	
		Theory (GGA+U)	Experiment
a	4.925		
c	13.54	13.68 [23], 13.85 [22]	13.566
μ	2.81	2.91 [23], 3.1 [22]	2.8
Bandgap	3.38	2.95 [23], 2.8 [22]	3.4

defect formation energies computed with GGA+U formalism, we utilized HSE hybrid functional. The bandgap of Cr₂O₃ predictions by the two widely used flavors of HSE, of HSE06 and HSE03, [38] hybrid functional, of 4.27 eV and 3.85 eV, respectively, were much higher than the experimental values of 3.2-3.4 eV. In order to lower the calculated bandgap closer to the experimental value of 3.4 eV, we modified the parameters of the HSE functional. We retained the 25% mixing of Hartree-Fock exchange at short range and increased the screening parameter till the computed bandgap matched with the experimental value. For bandgap fitting, we used a fixed cell size that was optimized with PBEsol+U approach in our previous studies. [23, 28] The bandgaps obtained with different screening parameters are listed in Table 1.

The results indicate that calculations with the screening parameter of 0.6 provide the best match between the computed and experimental bandgap. The primitive cell was then optimized with the chosen HSE parameters. The resulting cell dimensions, magnetic moment and bandgap are given in Table 2. Specifically, both a and c are smaller compared to those obtained using GGA+U and closer to the experimental values. Similarly, the computed magnetic moment of Cr has a better match with the experimental value. After relaxation, the bandgap increased negligibly from 3.377 eV to 3.384 eV. The resulting electronic density of states (DOS) of bulk Cr₂O₃ is given in Figure 1.

Cr-O phase diagram was evaluated by optimizing the Cr, O₂, and CrO₂ phases with HSE parameters identical to those used in the relaxation of Cr₂O₃ cell. The resulting phase diagram (given in SI Figure S1) yielded the formation energies of Cr₂O₃ and CrO₂ at -2.54 eV/atom and -2.17 eV/atom, respectively. The computed formation energy of Cr₂O₃ compares well with the corresponding experimental value of -2.35 eV/atom.

4.2. Defects

The number density of free electrons, n , is given by

$$n(T, E_F) = \int_{CBM}^{\infty} f_{FD}(E, T, E_F)g(E)dE, \quad (12)$$

where $g(E)$ is the density of states, f_{FD} is the Fermi-Dirac distribution function given by

$$f_{FD}(E, T, E_F) = \frac{1}{1 + e^{(E-E_F)/kT}}. \quad (13)$$

Similarly the number of free holes, p , is given by

$$p(T, E_F) = \int_{-\infty}^{VBM} (1 - f_{FD}(E, T, E_F))g(E)dE. \quad (14)$$

Substituting Eqns. 11, 12, and 14 into Eqn. 9, and by making T and p_{O_2} as free variables, we can solve for E_F in terms of T and p_{O_2} self-consistently. The resulting defect concentrations are given by

$$c^{X_0^q}(p_{O_2}, T) = c_0^{X_0^q} e^{-E_f^{X_0^q}(p_{O_2}, T)/kT}. \quad (15)$$

4. Results and Discussion

4.1. HSE Screening Parameter

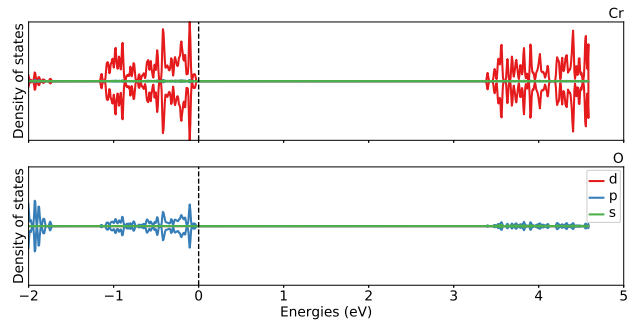


Figure 1: Electronic DOS of bulk Cr₂O₃ computed with HSE functional with 0.6 screening parameter.

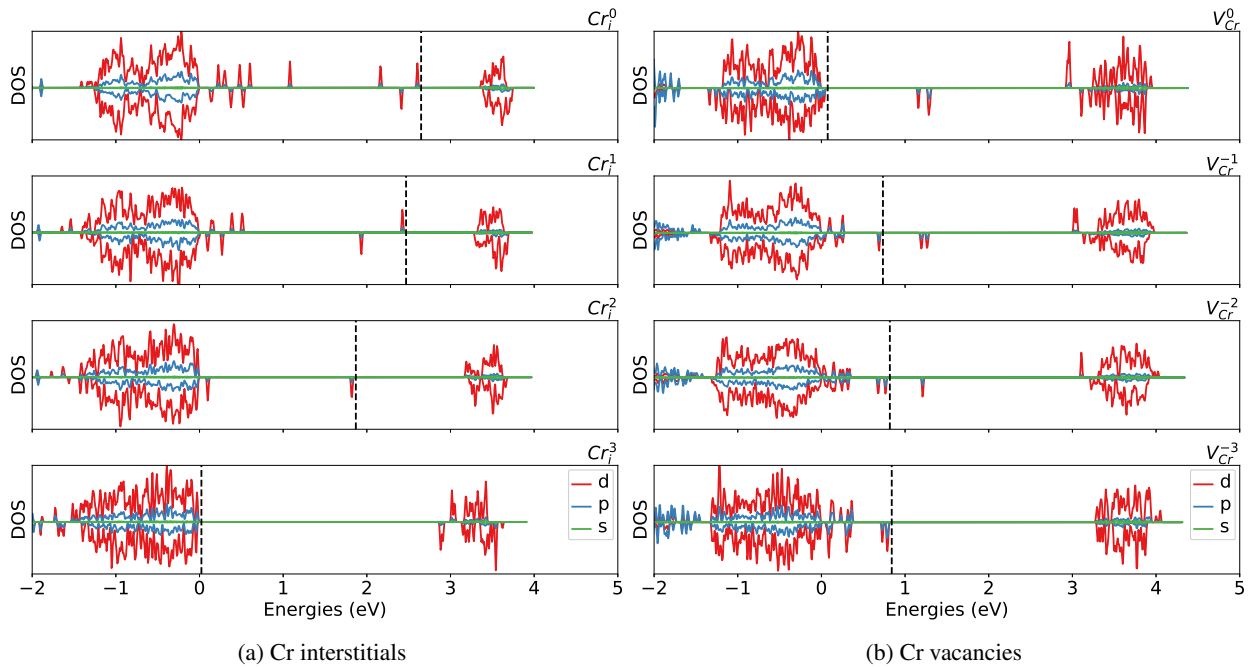


Figure 2: Orbital projected DOS averaged over all sites for interstitials in different charge states. Dashed vertical line marks the position of the Fermi level. The zero level has been fixed at the VBM.

Defect calculations were performed using a $2 \times 2 \times 1$ supercell containing vacancies and interstitials and generated from the optimized primitive cell. In addition to vacancies and interstitials, Cr vacancy triple defect (or split-vacancy) identified in our earlier work [23] was also considered. The ionic positions in the defect supercells were optimized under fixed volume and shape conditions.

To gain an understanding of how HSE affected defect properties, we evaluated electronic density of states (DOS), distribution of excess electrons and holes for charged defects, and the formation energies of the optimized defects.

4.2.1. Electronic Structure of Defects

Previous studies of defects in Cr_2O_3 mainly employed GGA+U method. Given that U and the width of the bandgap often have monotonic relationship U value is often fitted to recover experimental bandgap. The choice of the U-value not only affects the bandgap but also the position of the VBM and to a certain extent CBM with respect to the core bands. To get an understanding of the influence of U on the defect induced electronic states, we focus on the defect levels of the neutral Cr and O vacancies. In particular, in the studies of Lebreau et al., and Rak and Brenner, the U value of 5.0 eV within Dudarev formalism was used for Cr-3d electrons. According to the DOS of the vacancies reported in these two studies, neutral Cr vacancy

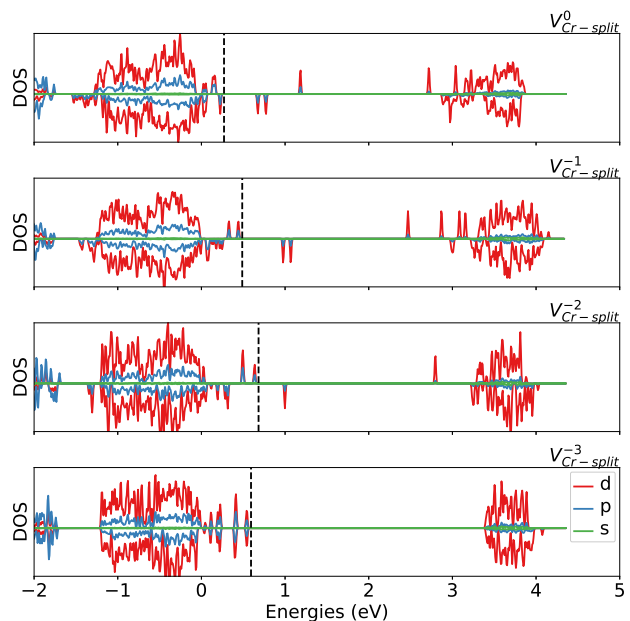


Figure 3: Orbital projected DOS averaged over all sites for Cr vacancy triple defects in different charge states. Dashed vertical line marks the position of the Fermi level. The zero level has been fixed at the VBM.

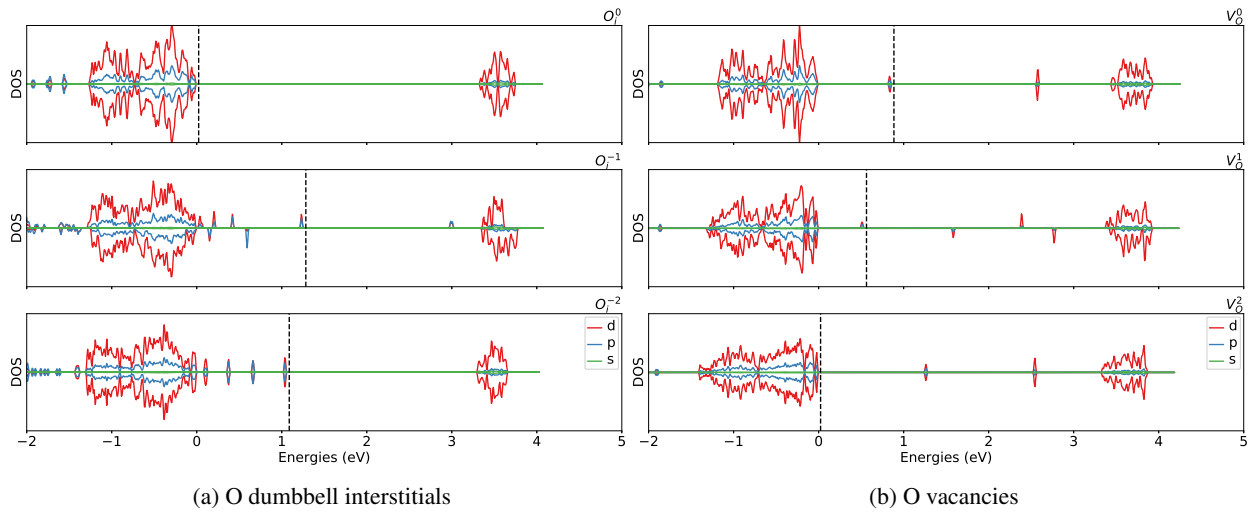


Figure 4: Orbital projected DOS averaged over all sites for O defects in different charge states. Dashed vertical line marks the position of the Fermi level. The zero level has been fixed at the VBM.

exhibits two defect levels, one that is slightly above the VBM (0.2 or 0.3 eV, respectively), and another that is unoccupied and at the bottom of the CBM. Differing from these studies, Gray et al. used $\{U, J\} = \{4.5, 1\}$ eV within the Liechtenstein formalism and Medasani et al. used $U=3.7$ eV within Dudarev formalism. Both studies indicate that V_{Cr} introduces multiple defect levels. Gray et al.'s results point to four distinct defect levels (with two of them very close to each other and slightly below the CBM) in the bandgap, and Medasani et al. reported 5 distinct defect levels. If defect levels that are energetically closer are grouped together, then Gray et al and Medasani et al's data predict the existence of three defect level zones: a) just above the VBM, b) 1 eV above the VBM, and c) just below the CBM. The HSE results confirm this pattern (Figure 2b). This indicates that U_{eff} of ~ 3.7 eV is able to describe defect levels of V_{Cr} more accurately at the GGA+U level of theory. For V_O^0 , HSE predicts two defect levels that are spin degenerate at 0.8 and 2.6 eV above VBM (Figure 4b). Similar electronic structure for V_O^0 was obtained in the study of Gray et al., where the spin degenerate levels are at 1.3 and 2.6 eV and in the study of Carey et al, who used $U_{Cr-3d} = 5$ eV and $U_{O-2p} = 5.5$ eV, where the corresponding defect levels are at 1 and 2 eV above the VBM. Medasani et al. instead observed no degeneracy, but the resulting four levels are still within the bandgap. In contrast, Lebreau et al. observed no defect levels within the bandgap for V_O . These results indicate that the energetic position of defect electronic states with respect to the VBM are highly dependent on the choice of U parameters and on the +U formalism selected. Comparison with the HSE results shows that although some GGA+U data qualitatively match the HSE results the difference is often quite noticeable especially for neutral vacancies. Interestingly, for charged defects such as V_{Cr}^{-3} , V_O^2 , and for interstitials, defect levels obtained from our GGA+U calculations are in good agreement with those obtained from HSE calculations (see Figures 2b-4a). It is noteworthy that unlike the study by Gray et al of native vacancies in Cr_2O_3 that assumed fixed defect levels in the bandgap independent of the defect charge state, our earlier GGA+U and the present HSE studies on vacancies and interstitials indicate that defect levels in the bandgap are not fixed but vary depending on the defect charge state.

4.2.2. Charge distribution

The distribution of the charge of excess hole(s) or electron(s) for the various charge states of the native vacancies and self-interstitials is shown in SI Fig. S2 - S5. These plots indicate that both holes and electrons are delocalized. This finding on the delocalization of the holes is consistent with the earlier studies [33, 46, 23]. However, comparison of charge distributions of Cr_i^1 and Cr_i^2 holes shows that delocalization is more pronounced when GGA+U is used.

4.2.3. 0-K Defect Formation Energies

After structure optimization, the spurious electrostatic interactions inherent in the periodic boundary formalism of charged defects were corrected using the anisotropic FNV (Freyssoldt, Neugebauer, and Vande Walle) method [47, 48]

(see Table S1 in SI for the resulting corrections). The charge transition levels of the defects with respect to the valence band maximum are presented in Table S2 in the SI. When compared to the corrected transition levels reported in our previous works, the corresponding transition levels obtained with HSE are overall at a higher Fermi level. Some of the transition levels such as Cr_i (3/2) transition, which is at 2.6 eV above the VBM, differ by nearly 1 eV (1.64 eV in Ref [28]). Further, HSE predicts that only +3 and +2 charge states are stable for Cr_i within the bandgap. On the other hand, the O_i (0/-2) transition level at 3.07 eV differs only by 0.14 eV from the corresponding transition level computed using GGA+U coupled with bandgap correction. This shows that while bandgap correction overall improves the position of the transition levels computed with GGA+U, the improved agreement between the HSE computed and bandgap corrected GGA+U formation energies is not systematic. The position of some transition levels such as O_i (0/-2) and V_O (1/0) are almost the same, while the position of other transition levels such as Cr_i (3/2) and V_O (2/1) exhibit differences that are greater than 0.4 eV when computed at the HSE and GGA+U levels of theory.

Table 3: Defect formation energies (in eV) of Cr_2O_3 with Fermi level (E_F) at the middle of the bandgap under O-rich conditions.

Defect	q	HSE	GGA+U [23, 28]
V_O	0	5.55	6.01
	1	5.62	6.34
	2	6.16	7.47
V_{Cr}	0	0.90	1.93
	-1	0.93	1.69
	-2	1.30	1.37
	-3	2.00	1.66
O_i	0	2.94	2.18
	-1	4.77	3.69
	-2	5.76	4.38
Cr_i	0	11.65	10.13
	1	9.58	8.82
	2	7.85	7.91
	3	6.92	7.97

theory, as reported in our previous works, [23, 28] and the defect formation energies computed at the HSE level of theory. We expect this approach to yield reliable activation energies at lower computational cost due to insensitivity of GGA+U defect migration barrier energies to the variation in U value[27].

The resulting self-diffusion coefficients are plotted as a function of temperature in Figure 6 at four different conditions: a) standard conditions (1 atm), b) moderate vacuum (1×10^{-8} atm), c) high vacuum (1×10^{-14} atm), and d) metal/metal oxide interface conditions. Electronic effects such as band bending and the finite electric field arising at the metal-metal oxide and vacuum-metal oxide interfaces are ignored in this study. The plots indicate that at O_2 partial pressure (p_{O_2}) of 1 atm, Cr has higher mobility than O. The difference in the mobilities is higher at lower temperatures. As p_{O_2} is reduced to 1×10^{-8} atm, O become the dominant diffusing species at temperatures higher than 1100 K. At lower temperatures (< 1100 K), Cr still has a higher mobility, but the magnitude of mobility difference is reduced. As p_{O_2} decreases further to 1×10^{-14} atm, O mobility becomes higher than that of Cr at even lower temperatures (800 K). At Cr/Cr_2O_3 interface, relative O mobility is significantly higher than that of Cr at all temperatures studied.

The dependence of 0K defect formation energies on the position of the Fermi level for both O-rich and Cr-rich conditions shows that not only transition levels, but also the formation energies differ between HSE and GGA+U even after corrections (Figure S7 in SI). At Cr-rich phase boundary, HSE predicts lower formation energies than GGA+U for the dominant Cr_i and V_O defects. At O_2 -rich phase boundary HSE predicted formation energies are lower for neutral Cr vacancies and higher for O_i . In contrast, for charged Cr vacancies, the HSE formation energies are in good agreement with those calculated using the GGA+U. These results validate our choice of using HSE to obtain more accurate formation energies needed for the calculation of self-diffusion coefficients

4.3. Self Diffusion Coefficients

We evaluated the self-diffusion of Cr and O species mediated by vacancies and interstitials along the diffusion pathways identified in earlier works [22, 23, 28]. Activation energies for defect migration are sum of transition state barrier energies computed at the the GGA+U level of

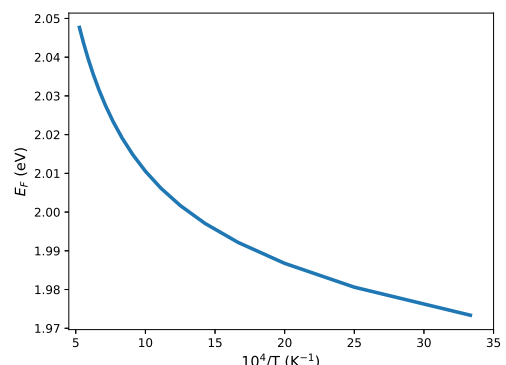


Figure 5: Fermi level in intrinsic Cr_2O_3 at Cr/Cr_2O_3 interface (Cr-rich condition) as a function of temperature.

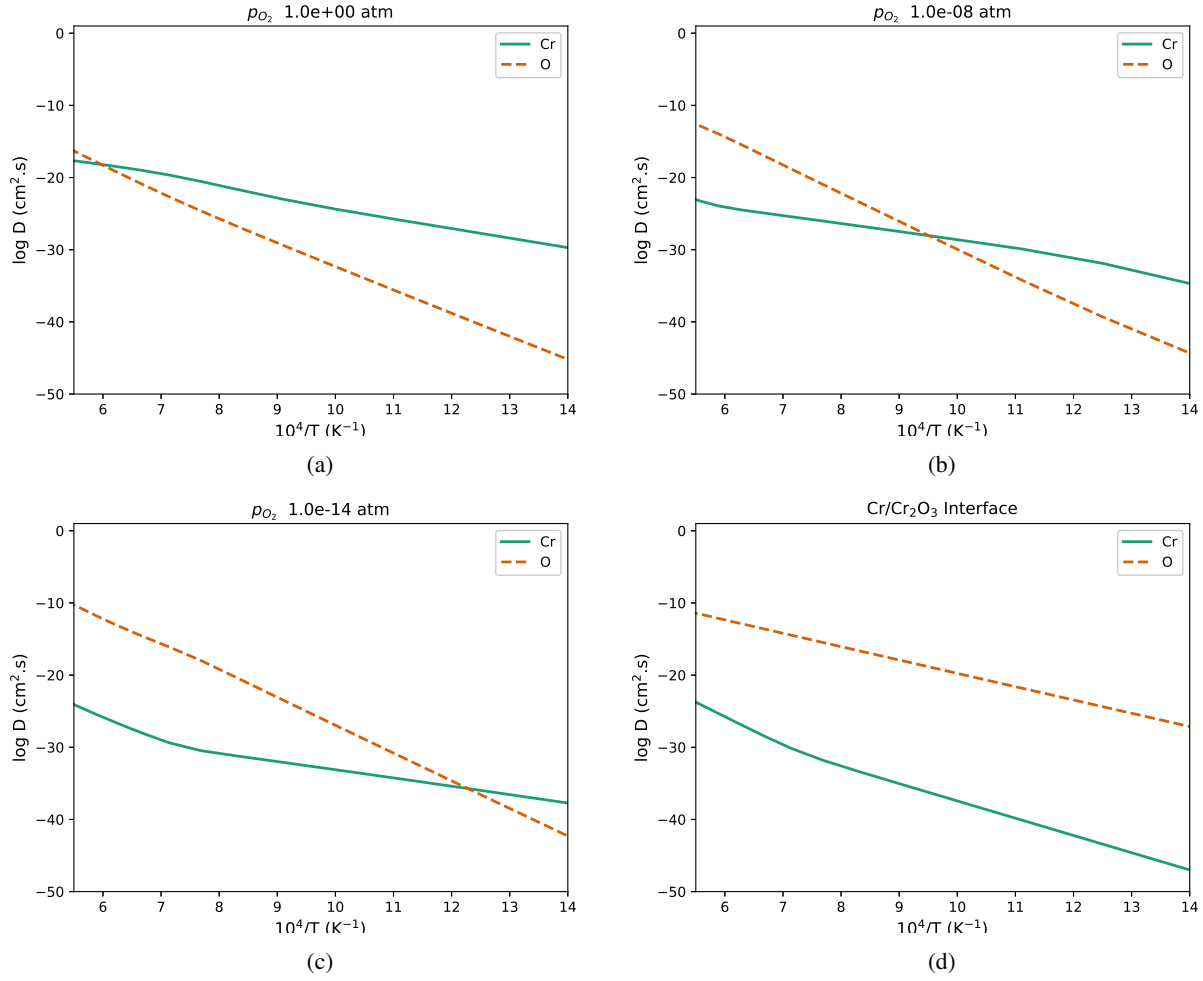


Figure 6: Self diffusion coefficients of Cr and O at vacuum/oxide interface at O_2 partial pressures of a) 1 atm, b) 1×10^{-8} atm, c) 1×10^{-14} atm, d) and at Cr/oxide interace.

Sabioni reported the experimental diffusion coefficients of Cr and O as $(2.2 - 7.2) \times 10^{-18} \text{ cm s}^{-2}$ and $(3.2 - 8.4) \times 10^{-18} \text{ cm s}^{-2}$ measured at 1300° C and 1100° C respectively under high vacuum conditions. The experimental diffusion coefficients reported by Sabioni et al. were nearly the same for Cr and O, and relatively independent of p_{O_2} . Sabioni proposed the surprising independence of the diffusion coefficients from p_{O_2} could be due to the presence of impurities in the Cr_2O_3 samples at around 1 ppm level. The resulting high concentration of extrinsic defects may have affected the diffusion coefficients in the Cr_2O_3 samples. While the diffusion coefficients reported by Sabioni could not be considered representative of intrinsic Cr_2O_3 , they could serve as higher limits on one of the diffusion coefficients by promoting the compensating defects of either Cr or O species. At 1373 K and at 1×10^{-14} atm, which are representative of experimental conditions used to measure O diffusion, the computed diffusion coefficient of O is found to be at $1 \times 10^{-18} \text{ cm s}^{-2}$. This indicates that O diffusion coefficient was not affected by the extrinsic defects. At 1573 K, the maximal value of Cr diffusion coefficient observed by us is at $1 \times 10^{-18} \text{ cm s}^{-2}$ (at standard conditions), which matches with the experimental value of Cr diffusion.

To identify the nature of the predominant defects facilitating the diffusion of each species we plotted the defect concentrations in Brouwer diagrams at different temperatures (Fig. 7). At low temperatures ($< 800 \text{ K}$), Cr vacancies (including Cr triple defects denoted as V_{Cr-TD}) have higher concentrations at all p_{O_2} . At 1200 K, the concentration of V_O is higher at p_{O_2} below 1×10^{-8} atm. Above 1×10^{-8} atm, Cr vacancies become the dominant defects. Due to the

high concentration of Cr vacancies at pressures close to 1 atm and temperatures above 1200 K, the self diffusion of Cr is equal to the one measured by Sabioni, suggesting that self-compensating Cr vacancies could be responsible for the high Cr diffusion coefficient (when compared to the intrinsic Cr diffusion coefficients at corresponding p_{O_2}). These results indicate that vacancies are the mediators of reported self-diffusion coefficients in Cr_2O_3 .

If the impurity concentration in Cr_2O_3 samples could be minimized to very low levels, Fig. 7c indicates that at high temperatures (> 1200 K) and low p_{O_2} ($< 1 \times 10^{-12}$ atm), V_O and Cr_i could be responsible for O and Cr diffusion respectively. However the relative mobility of O is very high in such cases, indicating again that vacancies dominate the diffusion process in Cr_2O_3 .

The Brouwer diagrams also reveal that it would be misleading to use commonly reported 0-K defect formation energies at the phase boundary edges to predict dominant defects responsible for experimentally measured diffusion coefficients. For example at Cr-rich boundary, the 0-K defect energy diagram (Figure S6 in SI) indicates that Cr_i could be the dominant defect if the Fermi level, E_F , lies between 1.5 to 1.9 eV. However, the allowed Fermi level range is only 1.97 – 2.04 eV (Figure 5) and neutral vacancies are the dominant defects. Fermi level variation is plotted as a function of p_{O_2} for different temperatures in Figure 8a. The plots indicate that Cr_2O_3 is intrinsically p-type at low temperatures and high p_{O_2} , where Fermi level can become as low as 1.2 eV. Under such conditions, the dominant defects are V_{Cr} (Figure S6 in SI). At low temperatures and low p_{O_2} , the Fermi level is around 1.75 eV making Cr_2O_3 slightly n-type intrinsically. Stoichiometry deviation plotted as a function of p_{O_2} in Figure 8(b) shows that the deviation is negligible in intrinsic Cr_2O_3 .

Figure 9 shows the anisotropic ratio of diffusion for Cr and O at various operational conditions. The results indicate that Cr_2O_3 basal plane is the preferential diffusion pathway for O under all conditions. For Cr, however, the preferred diffusion orientation is temperature dependent. At low temperatures, Cr diffuses mainly along the c -axis. The mode of diffusion switches to basal plane pathway at around 1200 K under high p_{O_2} . In ultra high vacuum conditions of $p_{O_2} \leq 1 \times 10^{-14}$ atm the primary mode of Cr diffusion switches back to c -axis at around 1600 K. Under such conditions, Cr diffusion coefficients along basal plane and c -axis become nearly the same.

5. Summary

Towards a comprehensive understanding of the diffusion processes in Cr_2O_3 , we computed the self diffusion coefficients and Brouwer diagrams in Cr_2O_3 . Diffusion coefficients were computed using the DFT at two accuracy levels and the Einstein random walk formalism. The defect formation energies were reevaluated with HSE hybrid functional for high accuracy, and were corrected for

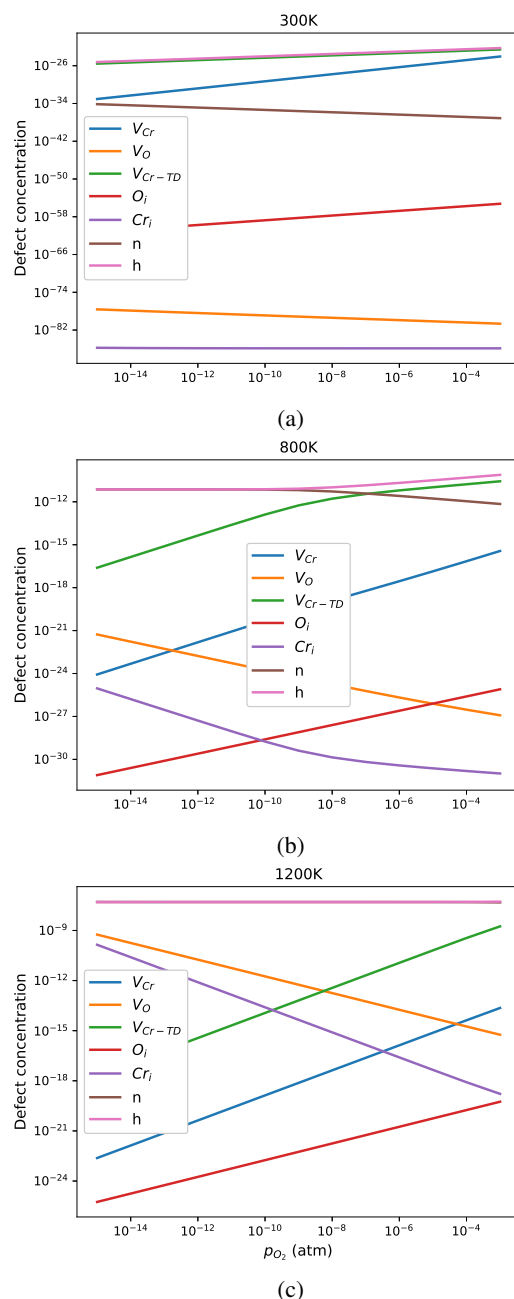


Figure 7: Brouwer diagrams depicting the defect concentrations vs. O_2 partial pressure in Cr_2O_3 for a) 300 K, b) 800 K, and c) 1200 K.

spurious electrostatic interaction errors arising in the periodic supercell method. The resulting self diffusion coefficients have a good agreement with the experimental data. Our results reveal that vacancies are primarily responsible for both Cr and O diffusion in intrinsic Cr_2O_3 . At high temperatures and low oxygen partial pressures, O has higher mobility. Cr has higher mobility at lower temperatures at moderate to high oxygen partial pressure. The preferred path for O diffusion is along the basal plane. Cr diffusion takes place along the c-axis at low temperatures and switches to basal plane at temperatures above 1200 K. The revealed mechanism for self-diffusion in Cr_2O_3 in a wide range of temperature and pressure conditions opens new avenues for the design of Cr_2O_3 materials.

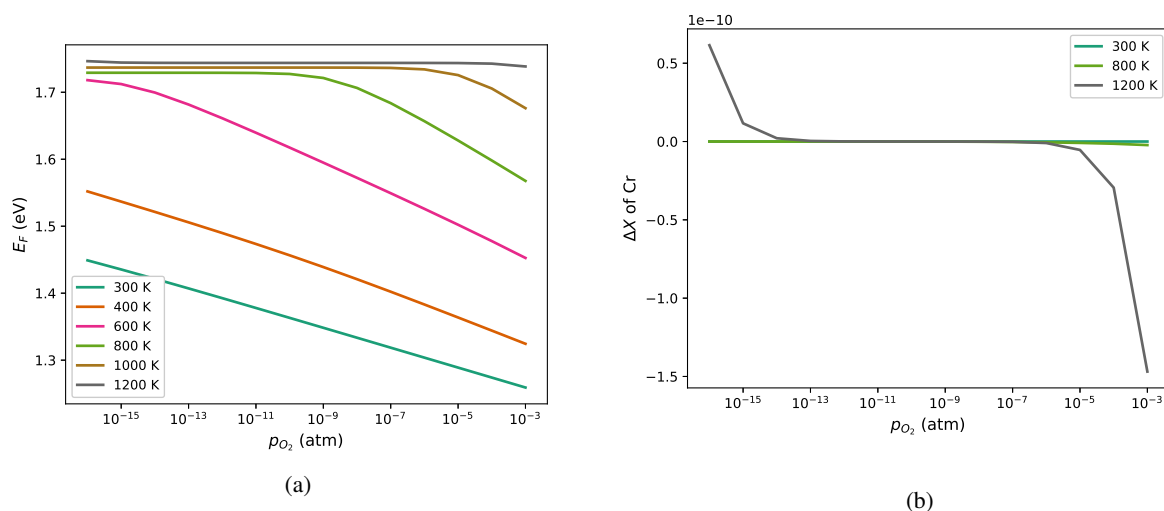


Figure 8: (a) Fermi level in intrinsic Cr_2O_3 , and (b) stoichiometry deviation expressed in terms of relative change in Cr composition from stoichiometry as functions of temperature and O_2 partial pressure.

Acknowledgement

This work was supported by the U.S. Department of Energy (DOE), Office of Science, Basic Energy Sciences, Materials Sciences and Engineering Division. Simulations were performed using PNNL Institutional Computing facility. PNNL is a multi-program national laboratory operated by Battelle for the U.S. DOE under Contract DEAC05-76RL01830.

References

- [1] Bates, M. K.; Jia, Q.; Ramaswamy, N.; Allen, R. J.; Mukerjee, S. Composite Ni/NiO- Cr_2O_3 Catalyst for Alkaline Hydrogen Evolution Reaction. *J. Phys. Chem. C* **2015**, *119*, 5467–5477.
- [2] Xie, Z.; Fan, J.; Cheng, Y.; Jin, L.; Hu, G.; Lu, J.; Luo, M. Cr_2O_3 Catalysts for Fluorination of 2-Chloro-3,3,3-Trifluoropropene to 2,3,3,3-Tetrafluoropropene. *Ind. & Eng. Chem. Res.* **2013**, *52*, 3295–3299.
- [3] Arca, E.; Kehoe, A. B.; Veal, T. D.; Shmeliov, A.; Scanlon, D. O.; Downing, C.; Daly, D.; Mullarkey, D.; Shvets, I. V.; Nicolosi, V.; Watson, G. W. Valence Band Modification of Cr_2O_3 by Ni-Doping: Creating a High Figure of Merit p-type TCO. *J. Mater. Chem. C* **2017**, *5*, 12610–12618.
- [4] Farrell, L.; Fleischer, K.; Caffrey, D.; Mullarkey, D.; Norton, E.; Shvets, I. V. Conducting Mechanism in the Epitaxial p-type Transparent Conducting Oxide Cr_2O_3 :Mg. *Phys. Rev. B: Condens. Matter Mater. Phys.* **2015**, *91*, 125202.
- [5] Mu, S.; Wysocki, A. L.; Belashchenko, K. D. Effect of Substitutional Doping on the Néel Temperature of Cr_2O_3 . *Phys. Rev. B: Condens. Matter Mater. Phys.* **2013**, *87*, 054435.
- [6] Pati, S. P.; Shimomura, N.; Nozaki, T.; Shibata, T.; Sahashi, M. Néel Temperature of Cr_2O_3 in Cr_2O_3 /Co Exchange-Coupled System: Effect of Buffer Layer. *J. Appl. Phys.* **2015**, *117*, 17D137.
- [7] Zurek, J.; Young, D.; Essuman, E.; Hnsel, M.; Penkalla, H.; Niewolak, L.; Quadackers, W. Growth and Adherence of Chromia Based Surface Scales on Ni-base Alloys in High- and Low- p_{O_2} Gases. *Mater. Sci. Eng.: A* **2008**, *477*, 259 – 270, 3rd International Conference on Spray Deposition and Melt Atomization (SDMA 2006) and the 6th International Conference on Spray Forming (ICSF VI).

- [8] Schreiber, D.; Olszta, M.; Saxey, D.; Kruska, K.; Moore, K.; Lozano-Perez, S.; Bruemmer, S. Examinations of Oxidation and Sulfidation of Grain Boundaries in Alloy 600 Exposed to Simulated Pressurized Water Reactor Primary Water. *Microsc. Microanal.* **2013**, *19*, 676–687.
- [9] Schreiber, D.; Olszta, M.; Bruemmer, S. Grain Boundary Depletion and Migration During Selective Oxidation of Cr in a Ni-5Cr Binary Alloy Exposed to High-Temperature Hydrogenated Water. *Scr. Mater.* **2014**, *89*, 41 – 44.
- [10] Brozek, V.; Pokorný, P.; Bouska, P.; Stouřil, J.; Mastný, L. Corrosion Properties of Chromia based Eco-friendly Coatings on Mild Steel. *Metalurgija* **2016**, *55*, 675–678.
- [11] Sabioni, A. C. S.; Huntz, A. M.; Philibert, J.; Lesage, B.; Monty, C. Relation Between the Oxidation Growth Rate of Chromia Scales and Self-Diffusion in Cr₂O₃. *J. Mater. Sci.* **1992**, *27*, 4782–4790.
- [12] Sabioni, A.; Lesage, B.; Huntz, A.; Pivin, J.; Monty, C. Self-Diffusion in Cr₂O₃ I. Chromium Diffusion in Single Crystals. *Philos. Mag. A* **1992**, *66*, 333–350.
- [13] Sabioni, A.; Huntz, A.; Millot, F.; Monty, C. Self-Diffusion in Cr₂O₃ II. Oxygen Diffusion in Single Crystals. *Philos. Mag. A* **1992**, *66*, 351–360.
- [14] Sabioni, A.; Huntz, A.; Millot, F.; Monty, C. Self-diffusion in Cr₂O₃ III. Chromium and Oxygen Grain-Boundary Diffusion in Polycrystals. *Philos. Mag. A* **1992**, *66*, 361–374.
- [15] Latu-Romain, L.; Parsa, Y.; Mathieu, S.; Vilasi, M.; Galerie, A.; Wouters, Y. Towards the Growth of Stoichiometric Chromia on Pure Chromium by the Control of Temperature and Oxygen Partial Pressure. *Corros. Sci.* **2017**, *126*, 238 – 246.
- [16] Huntz, A. M.; Tsai, S. C. Diffusion in Oxide Scales: Application to Cr₂O₃ Scales. *J. Mater. Sci. Lett.* **1994**, *13*, 821–825.
- [17] Kofstad, P.; Lillerud, K. Chromium Transport Through Cr₂O₃ Scales I. On Lattice Diffusion of Chromium. *Oxid. Met.* **1982**, *17*, 177–194.
- [18] Tsai, S.; Huntz, A.; Dolin, C. Growth Mechanism of Cr₂O₃ Scales: Oxygen and Chromium Diffusion, Oxidation Kinetics and Effect of Yttrium. *Mater. Sci. Eng. A* **1996**, *212*, 6–13.
- [19] Hoshino, K.; Peterson, N. Cation Self-Diffusion in Cr₂O₃. *J. Am. Ceram. Soc.* **1983**, *66*, c202–c203.
- [20] Schmucker, E.; Petitjean, C.; Martinelli, L.; Panteix, P.-J.; Lagha, S. B.; Vilasi, M. Oxidation of Ni-Cr Alloy at Intermediate Oxygen Pressures. I. Diffusion Mechanisms Through the Oxide Layer. *Corros. Sci.* **2016**, *111*, 467–473.
- [21] Catlow, C. R. A.; Corish, J.; Hennessy, J.; Mackrodt, W. C. Atomistic Simulation of Defect Structures and Ion Transport in α -Fe₂O₃ and α -Cr₂O₃. *J. Am. Ceram. Soc.* **1988**, *71*, 42–49.
- [22] Lebreau, F.; Islam, M. M.; Diawara, B.; Marcus, P. Structural, Magnetic, Electronic, Defect, and Diffusion Properties of Cr₂O₃: A DFT+U Study. *J. Phys. Chem. C* **2014**, *118*, 18133–18145.
- [23] Medasani, B.; Sushko, M. L.; Rosso, K. M.; Schreiber, D. K.; Bruemmer, S. M. Vacancies and Vacancy-Mediated Self Diffusion in Cr₂O₃: A First-Principles Study. *J. Phys. Chem. C* **2017**, *121*, 1817–1831.
- [24] Gray, C.; Lei, Y.; Wang, G. Charged Vacancy Diffusion in Chromium Oxide Crystal: DFT and DFT+U Predictions. *J. Appl. Phys.* **2016**, *120*, 215101.
- [25] Cao, P.; Wells, D.; Short, M. P. Anisotropic Ion Diffusion in α -Cr₂O₃: An Atomistic Simulation Study. *Phys. Chem. Chem. Phys.* **2017**, *19*, 13658.
- [26] Vaari, J. Molecular Dynamics Simulations of Vacancy Diffusion in Chromium(III) Oxide, Hematite, Magnetite and Chromite. *Solid State Ion.* **2015**, *270*, 10 – 17.
- [27] Rak, Z.; Brenner, D. W. First-Principles Investigation of Diffusion and Defect Properties of Fe and Ni in Cr₂O₃. *J. Appl. Phys.* **2018**, *123*, 155105.
- [28] Medasani, B.; Sushko, M. L.; Rosso, K. M.; Schreiber, D. K.; Bruemmer, S. M. First-Principles Investigation of Native Interstitial Diffusion in Cr₂O₃. *J. Phys. Chem. C* **2018**, *122*, 12984–12993.
- [29] Mehrer, H. *Diffusion in Solids*; Springer-Verlag: Berlin, 2007.
- [30] Liechtenstein, A. I.; Anisimov, V. I.; Zaanen, J. Density-Functional Theory and Strong Interactions: Orbital Ordering in Mott-Hubbard Insulators. *Phys. Rev. B: Condens. Matter Mater. Phys.* **1995**, *52*, R5467–R5470.
- [31] Dudarev, S. L.; Botton, G. A.; Savrasov, S. Y.; Humphreys, C. J.; Sutton, A. P. Electron-Energy-Loss Spectra and the Structural Stability of Nickel Oxide: An LSDA+U Study. *Phys. Rev. B: Condens. Matter Mater. Phys.* **1998**, *57*, 1505–1509.
- [32] Rohrbach, A.; Hafner, J.; Kresse, G. *Ab initio* Study of the (0001) Surfaces of Hematite and Chromia: Influence of Strong Electronic Correlations. *Phys. Rev. B: Condens. Matter Mater. Phys.* **2004**, *70*, 125426.
- [33] Kehoe, A. B.; Arca, E.; Scanlon, D. O.; Shvets, I. V.; Watson, G. W. Assessing the Potential of Mg-Doped Cr₂O₃ as a Novel p-type Transparent Conducting Oxide. *J. Phys. Chem. C* **2016**, *28*, 125501.
- [34] Cococcioni, M.; de Gironcoli, S. Linear Response Approach to the Calculation of the Effective Interaction Parameters in the LDA+U Method. *Phys. Rev. B: Condens. Matter Mater. Phys.* **2005**, *71*, 035105.
- [35] Kresse, G.; Hafner, J. *Ab initio* Molecular Dynamics for Liquid Metals. *Phys. Rev. B: Condens. Matter Mater. Phys.* **1993**, *47*, 558–561.
- [36] Kresse, G.; Hafner, J. *Ab initio* Molecular-Dynamics Simulation of the Liquid-Metal–Amorphous-Semiconductor Transition in Germanium. *Phys. Rev. B: Condens. Matter Mater. Phys.* **1994**, *49*, 14251–14269.
- [37] Kresse, G.; Furthmüller, J. Efficient Iterative Schemes for *Ab Initio* Total-Energy Calculations Using a Plane-Wave Basis Set. *Phys. Rev. B: Condens. Matter Mater. Phys.* **1996**, *54*, 11169–11186.
- [38] Krukau, A. V.; Vydrov, O. A.; Izmaylov, A. F.; Scuseria, G. E. Influence of the Exchange Screening Parameter on the Performance of Screened Hybrid Functionals. *J. Chem. Phys.* **2006**, *125*.
- [39] Blöchl, P. E. Projector Augmented-Wave Method. *Phys. Rev. B: Condens. Matter Mater. Phys.* **1994**, *50*, 17953–17979.
- [40] Kresse, G.; Joubert, D. From Ultrasoft Pseudopotentials to the Projector Augmented-Wave Method. *Phys. Rev. B: Condens. Matter Mater. Phys.* **1999**, *59*, 1758–1775.
- [41] Perdew, J. P.; Burke, K.; Ernzerhof, M. Generalized Gradient Approximation Made Simple. *Phys. Rev. Lett.* **1996**, *77*, 3865–3868.
- [42] Perdew, J. P.; Ruzsinszky, A.; Csonka, G. I.; Vydrov, O. A.; Scuseria, G. E.; Constantin, L. A.; Zhou, X.; Burke, K. Restoring the Density-Gradient Expansion for Exchange in Solids and Surfaces. *Phys. Rev. Lett.* **2008**, *100*, 136406.
- [43] Vineyard, G. H. Frequency Factors and Isotope Effects in Solid State Rate Processes. *J. Phys. Chem. Solids* **1957**, *3*, 121 – 127.
- [44] Youssef, M.; Yildiz, B. Intrinsic Point-Defect Equilibria in Tetragonal ZrO₂: Density Functional Theory Analysis with Finite-Temperature

Effects. *Phys. Rev. B: Condens. Matter Mater. Phys.* **2012**, *86*, 144109.

[45] Chase, M. W. J. *NIST-JANAF Thermochemical Tables, 4th Edition*; American Institute of Physics: New York, 1998.

[46] Lany, S.; Zunger, A. Assessment of Correction Methods for the Band-Gap Problem and for Finite-Size Effects in Supercell Defect Calculations: Case Studies for ZnO and GaAs. *Phys. Rev. B: Condens. Matter Mater. Phys.* **2008**, *78*, 235104.

[47] Freysoldt, C.; Neugebauer, J.; Van de Walle, C. G. Fully *Ab Initio* Finite-Size Corrections for Charged-Defect Supercell Calculations. *Phys. Rev. Lett.* **2009**, *102*, 016402.

[48] Kumagai, Y.; Oba, F. Electrostatics-Based Finite-Size Corrections for First-Principles Point Defect Calculations. *Phys. Rev. B: Condens. Matter Mater. Phys.* **2014**, *89*, 195205.

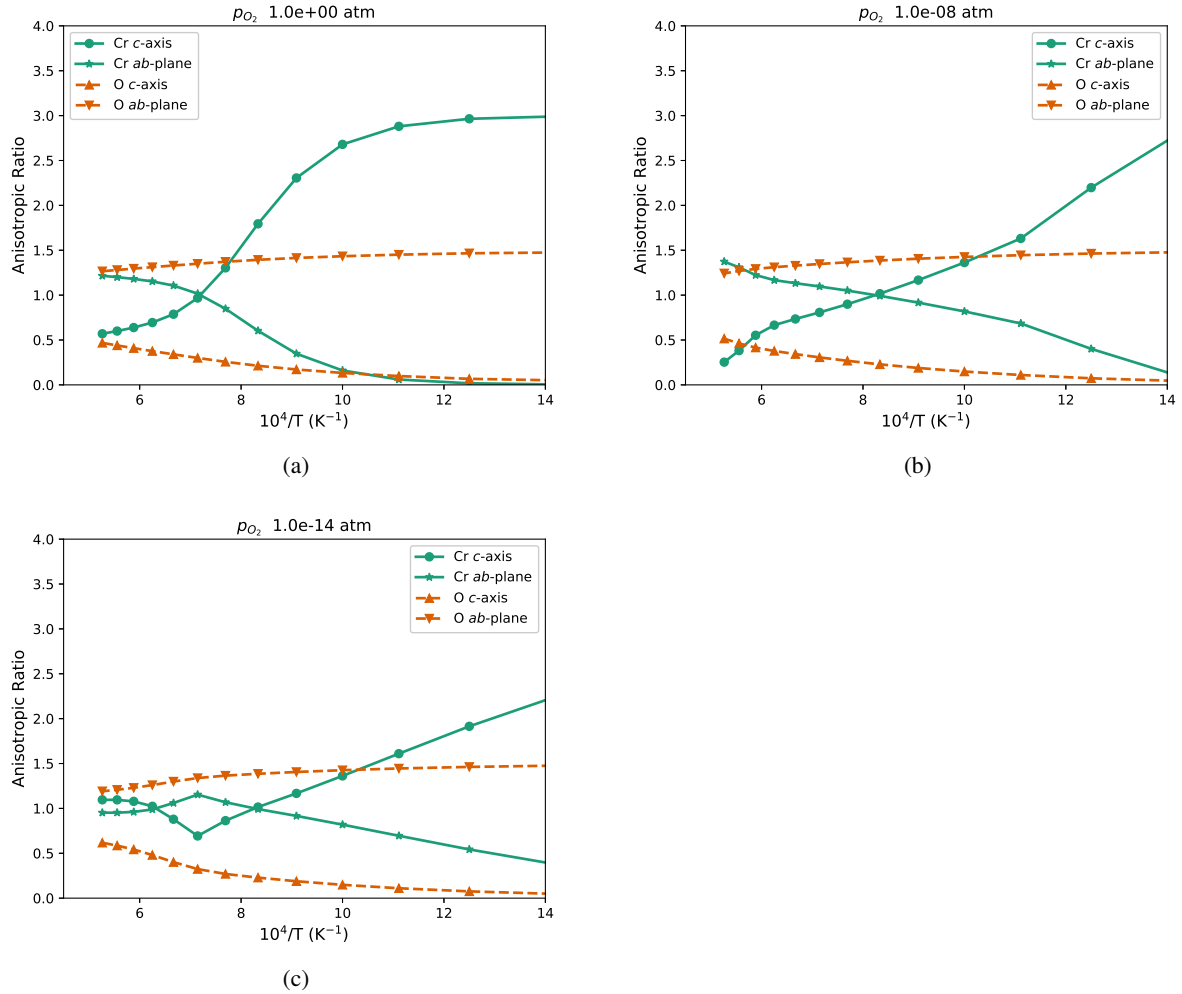


Figure 9: Anisotropic ratio of diffusion of Cr and O at vacuum/oxide interface at O₂ partial pressures of a) 1 atm, b) 1×10^{-8} atm, c) 1×10^{-14} atm.